Computers and Geotechnics 188 (2025) 107527

Contents lists available at ScienceDirect

Computers and Geotechnics

journal homepage: www.elsevier.com/locate/compgeo

# A hybrid discrete element method with adaptive contact treatment approach for modeling discontinuous rock masses

Je Kyum Lee, Jorge Loy-Benitez, Myung Kyu Song, Sean Seungwon Lee *

*Department of Earth Resources and Environmental Engineering, Hanyang University, 222 Wangsimni-ro, Seongdong-gu, Seoul 04763, Republic of Korea*

ARTICLE INFO

*Keywords:*
Adaptive contact modeling
Discontinuous rock mass
Force-based contact model
Hybrid discrete element method
Impulse-based contact model
Threshold velocity

ABSTRACT

The Discrete Element Method (DEM) has been widely used to simulate the mechanical behavior of discontinuous rock masses, particularly in underground environments; however, its applicability is often limited to specific contact conditions, such as quasi-static or dynamic interactions. To achieve broad applicability, this study presents a Hybrid Discrete Element Method (hDEM) that adaptively selects between different numerical schemes for contact treatment. The proposed method employs a threshold velocity based on the principle of energy conservation to distinguish between computational schemes at contact: a force-based method is applied to quasi-static contacts, while an impulse-based method is used for dynamic contacts. This approach enables hDEM to accommodate varying contact conditions within a unified framework. Several metrics, validated against theoretical solutions, demonstrate that the proposed approach yields accurate and stable results across different loading scenarios, addressing some of the limitations observed in conventional methods. The relative error of contact force was controlled within $5\times10^{-4}$ % in static tests and the mean absolute error of the velocity was recorded as $3.41\times10^{-3}$ m/s in dynamic tests. In a comparative simulation of tunnel excavation, hDEM achieved results similar to conventional DEM while reducing the number of convergence cycles by 65.4%, highlighting its efficiency and potential as a practical numerical tool for adaptive contact treatment of discontinuous rock masses.

## 1. Introduction

The stability of tunnels and underground structures is determined not only by continuous deformation in intact materials but also by discontinuous effects caused by structural features such as joints and faults, which play a particularly dominant role in blocky rock masses (Hoek and Brown, 1980). In 1979, Cundall and Strack developed the Discrete Element Method (DEM) to analyze the behavior of discontinuities, which has been extensively applied in various engineering fields (Cundall and Strack, 1979). DEM enables the explicit modeling of rock masses as independent blocks or particles, allowing for effective analysis of discontinuities such as joints and faults (Cundall, 1988; Hart et al., 1988). In the field of geotechnical engineering, this method has been established as a key tool for the analysis of discontinuous rock masses, particularly in highly confined conditions where quasi-static contacts are predominant, e.g., tunnel excavation or pillar stability analysis in underground mines (Jing and Hudson, 2002; Lisjak and Grasselli, 2014; Augrade et al., 2021).

At the same time, considerable efforts have been devoted to improving this approach, primarily addressing the computational costs that represent critical issues when performing these analyses. For instance, calculations based on penetration depth entail substantial computational demand with an increasing problem when solving large-scale models, leading to recurring concerns regarding the practical constraints of DEM (Paluszny et al., 2013; Lisjak and Grasselli, 2014). In addition, incorporating large-scale 3D simulations and coupling with thermodynamic or hydrodynamic calculations causes the simulation time to increase exponentially (Jing, 2003; Lemos, 2012; Wang et al., 2022). On the other hand, penetration depth-based calculations offer only conditional stability when small timesteps are used, making them a major contributor to the overall numerical burden (Augrade et al., 2021).

In recent years, there has been active research on applying hardware acceleration technologies to overcome the aforementioned computational limitations of DEM (Lubbe et al., 2020; Park et al., 2021; Duriez and Bonelli, 2021; Fukuda et al., 2021; Wang et al., 2024; Zhang et al., 2024; Lei et al., 2025). These studies primarily utilize frameworks such as OpenMP and CUDA to perform parallel computing with multi-core CPUs or general-purpose GPUs (GPGPUs), enabling efficient

* Corresponding author.
*E-mail address:* seanlee@hanyang.ac.kr (S.S. Lee).

https://doi.org/10.1016/j.compgeo.2025.107527
Received 29 April 2025; Received in revised form 30 June 2025; Accepted 26 July 2025
Available online 1 August 2025

**Nomenclature**

| Symbol | Description |
|---|---|
| $F$ | Force |
| $F_S$ | Shear force |
| $F_N$ | Normal force |
| $F_{max}$ | Maximum friction force |
| $F_d$ | Damping force |
| $M$ | Moment |
| $M_d$ | Damping moment |
| $K$ | Stiffness |
| $K_S$ | Shear stiffness |
| $K_N$ | Normal stiffness |
| $t$ | Time |
| $m$ | Mass |
| $I$ | Moment of inertia |
| $m_c$ | Collision mass |
| $u$ | Position, Direction |
| $\Delta u$ | Displacement |
| $\Delta u_{rel}$ | Relative displacement |
| $C_{scale}$ | Scale factor |
| $\dot{u}$ | Velocity |
| $\ddot{u}$ | Acceleration |
| $\theta$ | Angular position |
| $\dot{\theta}$ | Angular velocity |
| $\ddot{\theta}$ | Angular acceleration |
| $\varphi$ | Friction angle |
| $c$ | Cohesion |
| $\alpha$ | Damping constant of local damping |
| $R$ | Damping constant (restitution coefficient) |
| $J$ | Impulse |
| $n$ | Unit vector |
| $n_N$ | Normal unit vector |
| $n_S$ | Shear unit vector |
| $\xi_g$ | Global damping ratio |
| $\omega$ | Natural frequency |
| $E$ | Energy |
| $u_S$ | Elastic shear displacement |
| $u_N$ | Elastic normal displacement(penetration depth) |

processing of large-scale simulations and multi-physics couplings. For instance, Lei et al. (2025) developed a new contact detection algorithm using GPGPU to improve memory usage and computational efficiency, whereas Wang et al. (2024) leveraged OpenMP to model excavation with rock bolt support on modern CPUs. Fukuda et al. (2021) introduced a novel contact activation scheme for dynamic rock fracturing, and Zhang et al. (2024) expanded FDEM for elastoplastic-damage-fracture behaviors using improved GPU-parallelization.

While hardware-based approaches offer clear performance benefits, algorithmic improvements provide a complementary path that can enhance computational efficiency without relying on specific hardware configurations. One such approach is impulse-based dynamic simulation, also known as the momentum-exchange method, which computes contact interactions based on impulse(Hahn, 1988; Baraff, 1989; Cundall and Hart, 1992). Although this method may compromise some accuracy compared to conventional DEM, it offers a significant advantage in simulating contacts at high speed (Mirtich, 1996). Originally developed and widely used in animation and gaming applications, this method has recently attracted growing interest in the field of granular materials due to its computational efficiency (Lee, 2014; Lee and Hashash, 2015; Park et al., 2021). However, because it models all contacts as instantaneous collisions, impulse-based dynamic simulation has difficulty accurately capturing quasi-static contact behavior, particularly under highly confined conditions (Tan et al., 2024).

DEM and impulse-based dynamic simulation have inherent advantages and limitations. Given their complementary characteristics, a proper integration of these methods is expected to enable more accurate and efficient modeling of both static and dynamic behaviors in systems dominated by discontinuous deformation. Accordingly, this study proposes a new approach, namely the hybrid Discrete Element Method (hDEM), in which either DEM or the impulse-based method is selectively applied depending on the characteristics of contact. This paper consists of five major sections. The study begins by examining the theoretical foundations and key features of both DEM and the impulse-based method, described in Section 2. The definition of the proposed hDEM, along with the threshold velocity, which plays a central role in its framework, are presented in Section 3. Then, the proposed method is verified through preliminary numerical simulations conducted on a simplified two-block system, as well as a tunnel excavation scenario, reported in Section 4. Finally, the conclusion and remarks are described in Section 5. Based on these results, the computational efficiency and potential applicability of hDEM are evaluated, and directions for future research are discussed.

## 2. Theoretical background

DEM is widely used to analyze the mechanical behavior of discontinuous media. In this study, DEM is broadly categorized into the force-based method (FBM) and the impulse-based method (IBM), based on their physical interpretation of contact interactions; FBM relies on the spring-damper model, whereas IBM is based on the impulse-momentum principle. This fundamental difference directly influences their numerical behavior and applicability, resulting in distinct advantages and limitations.

Thus, a comparative analysis of FBM and IBM is presented in this chapter, focusing on their differences in contact mechanics, joint modeling, and damping strategies. The insight gained from this comparison provides the theoretical foundation and rationale for the adaptive contact treatment strategy introduced in the following chapter, where the complementary features of the two methods are systematically integrated.

### 2.1. Force-based method

First proposed by Cundall and Strack (1979), the FBM was originally developed to analyze the discontinuous behavior of rock mass (Cundall and Strack, 1979). The initial research defined contact only between disks, i.e., circular 2D bodies; then, later studies expanded the analysis by introducing contact models for polygonal blocks and three-dimensional objects (Barbosa-Carrilllo, 1990; Cundall, 1988; Hart et al., 1988). While DEM consists of contact management and mechanical calculations, this study focuses on the mechanical calculations only, which comprise the following three key processes: (1) contact mechanics, (2) the joint model, and (3) the equation of motion.

#### 2.1.1. Contact mechanics

In DEM, all contacts are considered as a spring model. The reaction force ($\Delta \boldsymbol{F}$), generated upon contact point C between two blocks A and B, is determined by the product of the joint stiffness ($K$) and the relative displacement ($\Delta \boldsymbol{u}_{rel}$). The relative displacement over a single time step ($\Delta t$) is calculated from the relative velocity ($\dot{\boldsymbol{u}}_{rel}$), and it can be decomposed into normal and shear components, where $\Delta \boldsymbol{u}_N$ and $\Delta \boldsymbol{u}_S$ denotes the relative displacement in the normal and shear directions, respectively, occurring during a single time step.

$$\Delta \boldsymbol{F} = K^{*}\Delta \boldsymbol{u}_{rel} \tag{1}$$

$$\Delta \boldsymbol{u}_{rel} = \dot{\boldsymbol{u}}_{rel}{}^{*}\Delta t = \Delta \boldsymbol{u}_N + \Delta \boldsymbol{u}_S \tag{2}$$

$$\dot{\boldsymbol{u}}_{rel} = \left(\dot{\boldsymbol{u}}_B + \dot{\boldsymbol{\theta}}_B \times \boldsymbol{u}_{B\to C}\right) - \left(\dot{\boldsymbol{u}}_A + \dot{\boldsymbol{\theta}}_A \times \boldsymbol{u}_{A\to C}\right) \tag{3}$$

$\dot{\boldsymbol{u}}_A$ and $\dot{\boldsymbol{\theta}}_A$ represent the translational and rotational velocities of block A, respectively, while $\boldsymbol{u}_{A\to C}$ denotes the moment arm from the centroid of block A to the contact point C.

The contact force is decomposed into normal ($\boldsymbol{F}_N$) and shear ($\boldsymbol{F}_S$) components, considering the contact plane, as expressed in Eqs. (4)-(6). $\widehat{n}_N$ is the normal direction unit vector and $\widehat{n}_S$ is the shear direction unit vector. $K_N$ is normal joint stiffness, and $K_S$ is shear joint stiffness. Finally, the resultant force ($\boldsymbol{F}_{Contact}$) and moment ($\boldsymbol{M}_{Contact}$) can be calculated using Eqs. (7) and (8).

$$\Delta \boldsymbol{F} = (\Delta \boldsymbol{F} \bullet \widehat{n}_N)\widehat{n}_N + (\Delta \boldsymbol{F} \bullet \widehat{n}_S)\widehat{n}_S = \Delta \boldsymbol{F}_N + \Delta \boldsymbol{F}_S \tag{4}$$

$$\boldsymbol{F}_N := \boldsymbol{F}_N + \Delta \boldsymbol{F}_N = \boldsymbol{F}_N + (K_N \Delta \boldsymbol{u}_N) \tag{5}$$

$$\boldsymbol{F}_S := \boldsymbol{F}_S + \Delta \boldsymbol{F}_S = \boldsymbol{F}_S + (K_S \Delta \boldsymbol{u}_S) \tag{6}$$

$$\boldsymbol{F}_{Contact} = \boldsymbol{F}_N + \boldsymbol{F}_S \tag{7}$$

$$\boldsymbol{M}_{Contact} = \boldsymbol{u}_{A\to C} \times \boldsymbol{F}_{Contact} \tag{8}$$

### 2.1.2. Joint model

A Joint model is a key element in DEM for simulating the behavior of discontinuities. Discontinuities exhibit complex interactions influenced by factors such as nonlinear shear strength, dilation occurring with shear displacement, and the effects of infill material and surface roughness. These factors play a crucial role in assessing the stability of underground structure, such as tunnels.

To capture the nonlinear behavior of joints, various joint models have been proposed. Notable research includes a model defining the relationship between normal stress and shear strength using friction angle and inclination angle (Patton, 1966), and a model incorporating JRC and JCS to account for roughness effects (Barton, 1973; Barton and Choubey, 1977). Other research has focused on the progressive degradation of shear strength due to shear displacement (Ladanyi and Archambault, 1969; Schneider, 1976; Barton, 1982; Plesha, 1987), and the influence of field-scale and lab-scale asperities on shear strength (Lee, 2003).

FBM has the advantage of accurately simulating complex discontinuity behavior by applying well-established joint models developed through extensive research. In this study, the Coulomb slip joint model, the most conventional model, was applied for the purpose of validating the new method. The shear component of the contact force, defined in Eq. (6), was modified by applying Eqs. (9), (10).

$$\boldsymbol{F}_S = \begin{cases} \dfrac{F_{max}}{|\boldsymbol{F}_S|}\boldsymbol{F}_S & , if F_{max} < |\boldsymbol{F}_S| \\ \boldsymbol{F}_S & , if F_{max} \geq |\boldsymbol{F}_S| \end{cases} \tag{9}$$

$$F_{max} = |\boldsymbol{F}_N|\tan(\varphi) + c \tag{10}$$

$F_{max}$ is the maximum friction force. $\varphi$ and $c$ represent the friction angle and cohesion of joint surface, respectively.

### 2.1.3. Equation of motion with mechanical damping

The motion of bodies is defined based on Newton's second law, considering both contact forces and external forces. Acceleration is calculated from the body force, contact forces, and moments obtained in Eqs. (7)-(8), followed by sequential updates of velocity and displacement. To simulate the dissipation of mechanical energy caused by various factors and enhance numerical stability, a damping term ($F_d$: damping force, $M_d$: damping moment) is incorporated into the equation of motion. In his early DEM research, Cundall proposed viscous damping (Cundall and Strack, 1979), but later improved it by proposing local damping, as described in Eqs. (11)-(14) (Cundall, 1987; Hart et al., 1988). While subsequent studies have explored more realistic damping models (Tsuji et al., 1992; Thornton, 1997; Stevens and Hrenya, 2005; Zhou et al., 2016), this study adopts the local damping approach, which is known to provide reliable numerical stability under quasi-static conditions.

$$\dot{\boldsymbol{u}}_A^{(t+\Delta t/2)} = \dot{\boldsymbol{u}}_A^{(t-\Delta t/2)} + \sum_i \left(\boldsymbol{F}_i - (\boldsymbol{F}_d)_i\right)\frac{\Delta t}{m_A} \tag{11}$$

$$\dot{\boldsymbol{\theta}}_A^{(t+\Delta t/2)} = \dot{\boldsymbol{\theta}}_A^{(t-\Delta t/2)} + \sum_i \left(\boldsymbol{M}_i - (\boldsymbol{M}_d)_i\right)\frac{\Delta t}{I_A} \tag{12}$$

$$(\boldsymbol{F}_d)_i = \alpha \sum \left|\boldsymbol{F}_i^{(t)}\right| sgn\left(\dot{\boldsymbol{u}}_A^{(t-\Delta t/2)}\right) \tag{13}$$

$$(\boldsymbol{M}_d)_i = \alpha \sum \left|\boldsymbol{M}_i^{(t)}\right| sgn\left(\dot{\boldsymbol{\theta}}_A^{(t-\Delta t/2)}\right) \tag{14}$$

$\dot{\boldsymbol{u}}$ is the transient velocity and $\dot{\boldsymbol{\theta}}$ is the angular velocity. $\dot{\boldsymbol{u}}_A^{(t-\Delta t/2)}$ and $\dot{\boldsymbol{\theta}}_A^{(t-\Delta t/2)}$ denotes the velocity of block A before contact forces are accounted for, while $\dot{\boldsymbol{u}}_A^{(t+\Delta t/2)}$ and $\dot{\boldsymbol{\theta}}_A^{(t+\Delta t/2)}$ is the velocity after they are applied. $m_A$ and $I_A$ is mass and moment of inertia of block A, respectively. $\alpha$ is damping coefficient for the local damping. $sgn(\dot{\boldsymbol{u}})$ represents the direction vector of $\dot{\boldsymbol{u}}$.

The magnitude of the damping force is proportional to the net nodal force, while its direction is opposite to the velocity. Since the magnitude of damping is determined regardless of velocity, a high damping effect can be achieved even at low velocities. This characteristic allows for stable simulation of static conditions with limited displacement, such as in underground spaces.

## 2.2. Impulse-based method

Impulse-based dynamic simulation was developed in the field of computer graphics to simulate rigid body collisions more efficiently and rapidly (Baraff, 1989; Hahn, 1988; Mirtich, 1996). Based on these advantages, it has been utilized across various fields beyond computer graphics and animation. In geotechnical engineering, it has been consistently applied in studies on soil and other granular materials (Lee and Hashash, 2015; Izadi and Bezuijen, 2018; Park et al., 2021).

### 2.2.1. Contact mechanics

IBM considers contact as an instantaneous collision and computes the resultant velocity change, whereas FBM assumes continuous contact and emphasizes precise modeling of the relationship between contact forces and displacement. The impulse ($J$) is used to determine post-impact velocities and defined by Eqs. (15) and (16), which include restitution coefficient ($R$) to account for energy dissipation during contact. The velocity changes of bodies due to collision are defined by Eqs. (17) and (18). Detailed derivation process can be found in the references (Baraff, 1997a, 1997b; Kavan, 2003).

$$J = m_c \Delta \dot{\boldsymbol{u}}_{rel} \bullet \widehat{n}_J = -(R+1)m_c \dot{\boldsymbol{u}}_{rel} \bullet \widehat{n}_J \tag{15}$$

$$m_c = 1 \Big/ \left(\frac{1}{m_A} + \frac{\widehat{n}_J \bullet ((\boldsymbol{u}_{A\to C} \times \widehat{n}_J) \times \boldsymbol{u}_{A\to C})}{I_A} + \frac{1}{m_B} + \frac{\widehat{n}_J \bullet ((\boldsymbol{u}_{B\to C} \times \widehat{n}_J) \times \boldsymbol{u}_{B\to C})}{I_B}\right) \tag{16}$$

$$\dot{\boldsymbol{u}}_A^{+} = \dot{\boldsymbol{u}}_A^{-} + \frac{J\widehat{n}_J}{m_A} \tag{17}$$

$$\dot{\boldsymbol{\theta}}_A^+ = \dot{\boldsymbol{\theta}}_A^- + J\frac{\boldsymbol{u}_{A\to C} \times \widehat{n}_J}{m_A} \tag{18}$$

$m_c$ in Eq. (15) represents the collision mass, which is defined as in Eq. (16). $\dot{\boldsymbol{u}}_{rel}$ denotes the relative velocity at the contact point 'C' just before impact. $\widehat{n}_J$ is the direction vector of the impulse. $\dot{\boldsymbol{u}}_A^-$ and $\dot{\boldsymbol{\theta}}_A^-$ are the velocities of block 'A' before contact, and $\dot{\boldsymbol{u}}_A^+$ and $\dot{\boldsymbol{\theta}}_A^+$ are the velocities after contact.

As can be seen in Eqs. (15) and (16), the impulse is determined by the mass of bodies and their relative velocity at the contact point. In contrast to FBM, which relies on penetration depth, IBM is less sensitive to timestep size, improving numerical stability in simulations. However, the lack of consideration for penetration depth implies that any penetration errors that arise cannot be inherently corrected. To mitigate this issue, supplementary techniques, such as the position correction technique (Catto and Park, 2005; Catto, 2009; Lee and Hashash, 2015), which modifies velocity or displacement to eliminate normal overlap ($u_N$), must be employed, as outlined in Eq. (19).

$$\Delta\dot{\boldsymbol{u}}_A = \frac{u_N}{\Delta t}\widehat{n}_N \tag{19}$$

#### 2.2.2. Joint model

IBM accounts for instantaneous velocity changes during collision events. This characteristic is also reflected in the joint model, which focuses on calculating immediate motion changes by collisions rather than simulating the detailed nonlinear behavior at contact. Consequently, numerous studies have adopted a simplified approach that relies solely on normal stress and friction angle (Lee and Hashash, 2015; Izadi and Bezuijen, 2018; Li et al., 2021; Tan et al., 2024). In this study, Eq. (9) was employed instead of simplified form as the joint model within the IBM framework.

#### 2.2.3. Equation of motion with mechanical damping

The global damping applied in IBM is defined by Eqs. (20)-(22) (Lee and Hashash, 2015). This method determines the damping magnitude in proportion to the velocity of the body, effectively controlling excessive velocity and facilitating the gradual convergence to a stationary state.

$$\dot{\boldsymbol{u}} := \dot{\boldsymbol{u}}(1 - \alpha_d\Delta t) \tag{20}$$

$$\dot{\boldsymbol{\theta}} := \dot{\boldsymbol{\theta}}(1 - \alpha_d\Delta t) \tag{21}$$

$$\alpha_d = 2\xi_g\omega_{avg} \tag{22}$$

$\alpha_d$ is viscous global damping factors, $\xi_g$ is the global damping ratio and $\omega_{avg}$ is the average natural frequency of the system.

### 2.3. Theoretical insights into FBM and IBM

Both FBM and IBM are grounded in distinct physical principles, ensuring their theoretical validity. FBM models rigid body behavior based on spring-damper model, whereas IBM relies on the impulse-momentum theorem. These two approaches have evolved in distinct fields with unique objectives, which have led to fundamental differences in their treatment of contact mechanics, damping mechanisms, and strategies for numerical stability. These differences directly influence the scope of application and result in variations in their suitability for specific engineering problems.

FBM employs a spring-damper model to define contact mechanics, allowing for a certain degree of penetration. This approach provides a technical foundation for detailed simulation of the complex interactions between rock blocks. However, simulations relying on time discretization can induce unrealistic penetration depth, posing a potential risk of numerical instability (Mirtich, 1996). Thus, an extremely small timestep is required to ensure numerical stability, which consequently increases computational costs.

IBM defines contact using the concept of impulse which is calculated based on the masses, moment of inertia, and pre-collision velocity of the two colliding bodies. This approach offers a significant computational advantage, as post-collision velocities can be determined within a single cycle calculation. Furthermore, since impulse calculation does not incorporate penetration depth, IBM is relatively less sensitive to the degree of overlap between bodies. As a result, it ensures numerical stability by maintaining consistency in the results even when relatively large timesteps are used.

One of the primary challenges associated with IBM lies in the accurate modeling of static equilibrium (Tan et al., 2024). By treating all contacts as instantaneous collisions resolved within a single timestep, IBM represents even persistent contact states as a sequence of discrete, impulsive events. While this enables efficient simulation of dynamic interactions, it may reduce the capability of the method to simulate gradual force evolution, such as elastic shear deformation, dilation, and progressive mobilization of normal and shear resistance, which are critical features of quasi-static contacts along discontinuities. Additionally, this study notes with concern that under constrained conditions, the position correction technique used to compensate for penetration errors may distort the stress equilibrium between bodies or induce unintended movement in constrained bodies by adjusting displacement or velocity. As a result, IBM has inherent limitations in accurately capturing contact behavior in statically constrained conditions, such as in high-stress underground rock masses.

To summarize, FBM excels in accurately modeling contact under static equilibrium and quasi-static conditions, whereas IBM is highly efficient in simulating high-speed impact. However, real-world engineering problems often involve complex load interactions rather than being purely static or dynamic. Therefore, distinguishing contact types and selectively applying FBM or IBM accordingly can offer notable benefits in analyzing complex geotechnical systems exhibiting diverse contact behaviors.

## 3. Hybrid DEM

This study introduces a Hybrid Discrete Element Method (hDEM) that integrates the advantages of the Force-based Method (FBM) and the Impulse-based Method (IBM). The fundamental concept of hDEM is to classify contact states and selectively apply the most suitable method for each state. To achieve this, hDEM incorporates three key procedures: (1) Contact classification, in which the contact state is classified to determine whether IBM or FBM should be applied; (2) Impulse conversion, where the impulse calculated via IBM is converted into an equivalent contact force for compatibility with FBM; and (3) Conditional damping, in which damping schemes are applied according to the classified contact state.

As a preliminary study intended to validate the conceptual feasibility of hDEM, the analysis is limited to two-dimensional problems, with the discrete bodies modeled as polygonal blocks to represent the rock medium.

### 3.1. Threshold velocity ($\dot{\boldsymbol{u}}_{th}$) and contact classification

In previous impulse-based dynamic simulations, as implemented in IBM, velocity-based contact classification has been commonly adopted to distinguish between resting and dynamic contacts (Baraff, 1997a; Kavan, 2003; Lee and Hashash, 2015). In these approaches, contact is typically considered dynamic when the relative velocity ($\dot{\boldsymbol{u}}_{rel}$) exceeds a small numerical tolerance ($\varepsilon$), and resting otherwise.

$$\left|\dot{\boldsymbol{u}}_{rel}\right| > \varepsilon \tag{23}$$

Based on this approach, the present study introduces a threshold velocity ($\dot{u}_{th}$) as a physically interpretable criterion for contact classification, serving as an alternative to conventional numerical tolerances, thereby determining whether FBM or IBM should be applied to a given contact.

$$\left|\dot{\boldsymbol{u}}_{rel}\right| > \dot{u}_{th} \tag{24}$$

Fig. 1 schematically illustrates how the threshold velocity is applied for contact classification. If the relative velocity at a contact is lower than the threshold velocity, the contact is classified as continuous contact (low-velocity), and FBM is applied for contact calculation (FB-hDEM). Conversely, if the relative velocity exceeds this threshold, the contact is categorized as an instantaneous collision (high-velocity), and IBM is used (IB-hDEM).

The threshold velocity is defined as the maximum relative velocity that can occur during static contact due to gravitational acceleration and the release of stored elastic energy. This definition is based on the assumption that block motion is governed solely by gravity and contact forces, which are the only sources of velocity change in mechanical DEM simulations.

The elastic component of threshold velocity is derived by assuming an idealized case in which the stored elastic energy in a compressed contact spring is fully converted into kinetic energy. Without accounting for energy loss due to damping, the resulting velocity can be interpreted as the upper bound for static contact behavior. By combining this elastic upper bound with the gravitational component, which accounts for the constant velocity increment caused by gravity regardless of the contact regime, the threshold velocity provides a conservative criterion for identifying dynamic-dominant contacts.

According to the above definition, the threshold velocity ($\dot{u}_{th}$) can be expressed as a function of the gravity-induced velocity ($\dot{u}_{gravity}$), the contact spring-induced velocity ($\dot{u}_{elastic}$), and a scaling factor ($C_{scale}$) for

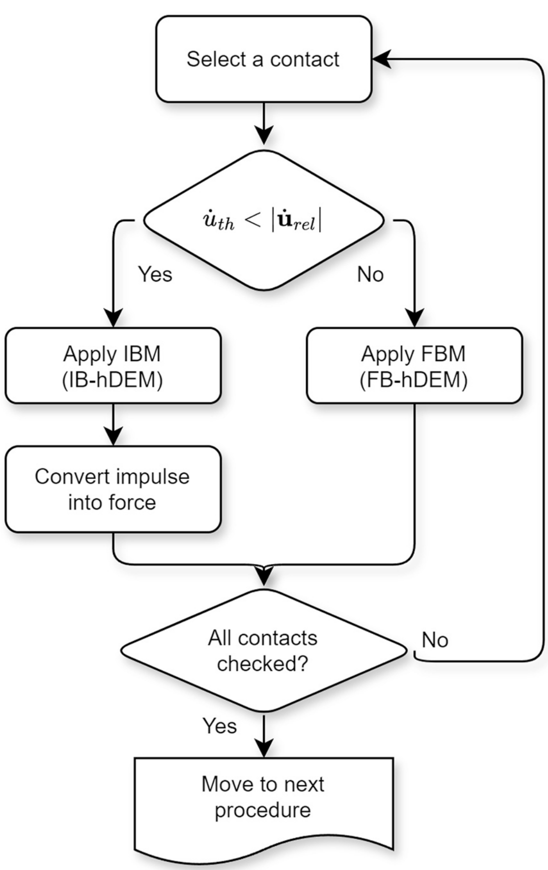


**Fig. 1.** Contact classification using threshold velocity ($\dot{u}_{th}$).

numerical stability, as shown in Eq. (25). In this formulation, $\dot{u}_{gravity}$ denotes the velocity change per unit timestep ($\Delta t$) due to gravitational acceleration ($\ddot{\boldsymbol{u}}_g$), as given in Eq. (26), and $\dot{u}_{elastic}$ represents the maximum velocity attainable from full conversion of stored elastic energy into kinetic energy, as in Eq. (27). A detailed derivation of $\dot{u}_{elastic}$ is provided in appendix A.

$$\dot{u}_{th} = C_{scale}{}^{*}\left(\dot{u}_{gravity} + \dot{u}_{elastic}\right) \tag{25}$$

$$\dot{u}_{gravity} = \Delta t\left|\ddot{\boldsymbol{u}}_g\right| \tag{26}$$

$$\dot{u}_{elastic} = \sqrt{\left|\frac{K_N|\boldsymbol{u}_N|^2}{m_{c,N}}\right| + \left|\frac{K_S|\boldsymbol{u}_S|^2}{m_{c,S}}\right|} \tag{27}$$

In Eq. (27), $\boldsymbol{u}_N$ represents the penetration depth in the normal direction of the contact surface, while $\boldsymbol{u}_S$ denotes the elastic deformation in the shear direction. The second term on the right-hand side of Eq. (27) corresponds to the elastic energy stored due to shear displacement, and $|\boldsymbol{u}_S|$ must not exceed $F_{max}/K_S$, where $F_{max}$ is the maximum shear friction force and $K_S$ is the shear stiffness. $m_{c,N}$ and $m_{c,S}$ are the collision mass in the normal and shear directions, respectively.

The scale constant ($C_{scale}$) is introduced to ensure numerical stability during the initial phase of the simulation, particularly in layered block structures. In such configurations, blocks settle sequentially from the bottom layer upward. During this process, the upper-layer blocks experience slightly longer fall distances, leading to higher initial velocities, which may inadvertently trigger the transition to IB-hDEM. As these unintended transitions can reduce computational efficiency, the scale constant, defined as the model-to-block dimension ratio, is introduced as a stabilization coefficient, as presented in Eq. (28).

$$C_{scale} = \frac{Width_{model}}{Width_{block}}\frac{Height_{model}}{Height_{block}} \tag{28}$$

All components of the threshold velocity ($\dot{u}_{th}$) can be obtained with minimal computational effort. $C_{scale}$ is an invariant and can be computed during the preprocessing stage. $\dot{u}_{gravity}$ also remains constant for a fixed timestep. The terms $|\boldsymbol{u}_N|$, $|\boldsymbol{u}_S|$, and $m_c$ are inherently computed during the contact force calculation, meaning that the computing $\dot{u}_{elastic}$ does not incur significant additional costs. Consequently, the overall overhead associated with determining the threshold velocity is minimal and does not impose a substantial burden on simulation performance.

### 3.2. Impulse to force conversion

Contacts in IB-hDEM are treated as instantaneous collisions within a single timestep. Accordingly, the resulting impulse can be converted into an equivalent average force ($F_J$) and acceleration ($\ddot{u}_j$) as in Eq. (29) and (30).

$$J = F_J\Delta t = m\ddot{u}_j\Delta t \tag{29}$$

$$\ddot{u}_j = \frac{J}{m\Delta t} \tag{30}$$

The appropriate timestep selection is crucial for accurately capturing the dynamic behavior of the system. In this study, the time interval is determined based on the system's natural frequency ($\omega_{max}$), as expressed in Eq. (31), suggested by Cundall (Cundall and Strack, 1979). A FRAC value was set to 0.1. However, in the numerical examples presented in the following chapter, a simplified value close to that calculated by Eq. (32) was adopted for convenience in verification.

$$\Delta t \le \Delta t_{cr} = \frac{2}{\omega_{max}} = 2\sqrt{\frac{m_{min}}{K_n}} \tag{31}$$

$$\Delta t = FRAC \bullet 2\sqrt{\frac{m_{min}}{2K_{max}}} \tag{32}$$

$m_{min}$ is the smallest block mass in the system. $K_{max}$ is the largest normal or shear joint stiffness.

### 3.3. Conditional damping

A unified damping strategy is required to effectively attenuate both FBM and IBM computations. Accordingly, hDEM adopts a conditional damping scheme in which different damping methods are applied depending on the contact state of each block: (1) For blocks with one or more IBM-based contact (i.e., high-velocity), velocity-based damping (Eqs. (10)–(13)) is applied; (2) For blocks with only FBM-based contacts, force-based damping (Eqs. (20)–(22)) is applied; and (3) For free-falling blocks without any contact, no damping is applied. This strategy ensures that the most suitable damping is applied depending on the physical state, thereby enhancing numerical stability during transitions between the two calculation schemes.

### 3.4. Conceptual overview of the proposed hDEM

The proposed hDEM is designed to improve numerical efficiency and accuracy by selectively applying contact-specific computational schemes. IB-hDEM addresses high-velocity collisions through efficient impulse-based treatment, whereas FB-hDEM captures quasi-static contact behavior in detail using force-based calculations. The conditional damping strategy further enables appropriate energy dissipation based on the contact states of individual blocks, contributing to a more stable representation of system behavior. Overall, this framework offers a unified modeling approach for systems involving both static and dynamic contact interactions.

## 4. Numerical experiment

A series of numerical simulations was conducted to verify the numerical performance of hDEM and assess its applicability to practical geotechnical problems. The validation strategy followed a systematic progression: (1) static contact verification to examine quasi-static behavior, (2) dynamic contact verification for high-velocity impacts, (3) energy continuity analysis during regime transitions, and (4) tunnel excavation simulation for practical geotechnical applications. This approach was designed to evaluate the fundamental mechanisms of hDEM and demonstrate its applicability for discontinuous rock mass modeling, the target geotechnical domain, with emphasis on accurate contact treatment under varying mechanical conditions. The performance of hDEM was evaluated by comparison with FBM and IBM applied independently under identical conditions.

As mentioned earlier, all simulations were two-dimensional with polygonal blocks, and all methods (hDEM, FBM, and IBM) were implemented using C++ code developed by the author.

### 4.1. Static condition test

To verify the implementation of vertical and shear contact forces under static equilibrium, a simple system was modeled, in which a single block was placed on a ground block, as shown in Fig. 2. All material properties, including block density, joint normal stiffness, shear stiffness, friction angle, and cohesion, were defined in Table 1. For simplicity, the upper block (Block 1) was modeled as a 1 m by 1 m square, and the ground block was fixed by applying displacement constraints. The timestep ($\Delta t_{cr}$) calculated using Eq. (32) was 8.78 × $10^{-5}$ sec. However, as mentioned earlier, a simplified value of 5.0 × $10^{-5}$ sec was applied for convenience in this verification example.

Gravity continuously acts as a body force, and after 5,000 cycle, an additional body force equivalent to an acceleration of 9.4 m/s$^2$ in the positive x-direction was applied. To ensure that contact was fully maintained, only the translational velocity component was considered, excluding rotational effects. This approach was adopted to verify pure shear contact behavior without the influence of moment-induced rotations. By constraining rotational motion, the resultant shear force directly corresponded to the applied body force, preventing unnecessary variations due to moment effects.

Until cycle 5000, the contact force between the two blocks corresponds to the self-weight of Block 1, which is theoretically 26,487 N. The contact impulse, obtained by multiplying the contact force by the timestep, is calculated as 1.32435 $N \bullet s$.

The results of all three methods converged to the theoretical value (Fig. 3). Applying FBM only, relatively large contact normal forces occurred initially, followed by gradual convergence to the theoretical

**Table 1**
Model properties for static test.

| Properties | | Unit | Value |
|---|---|---|---|
| Density | | Kg/m3 | 2,700 |
| Joint normal stiffness | | Pa/m | 7 × $10^9$ |
| Joint shear stiffness | | Pa/m | 5 × $10^8$ |
| Friction angle | | ° | 30 |
| Cohesion | | Pa | 1 × $10^4$ |
| Damping coefficient | R | – | 0.1 |
| | α | – | 0.8 |

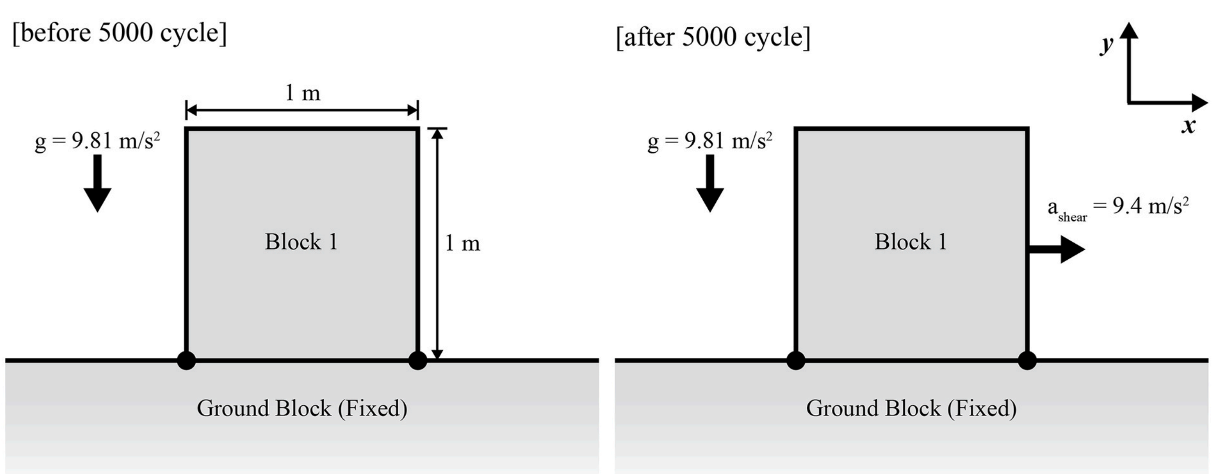


**Fig. 2.** Model description for static contact.

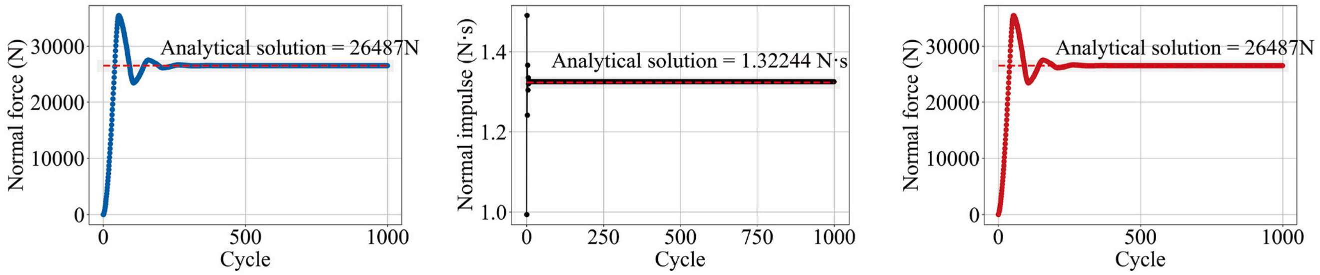


**(a) FBM** **(b) IBM** **(c) hDEM**

**Fig. 3.** Normal component of contact force and impulse.

value over approximately 300 cycles (Fig. 3-a). The hDEM showed a similar behavior to FBM (Fig. 3-c), as the initial velocity was zero and contact with the ground block generated immediately, keeping the velocity of Block 1 close to zero. As a result, the contact was classified as low-velocity, and force-based contact calculations (FB-hDEM) were applied within the hDEM framework. In contrast, the IBM-only simulation reached the theoretical value within 10 cycles, showing a significantly faster convergence rate than the other two methods (Fig. 3-b). These results clearly highlight the difference in how FBM and IBM simulate contact behavior: FBM models contact using a spring-based approach, where contact forces gradually accumulate to reach equilibrium, whereas IBM directly computes and applies the impulse corresponding to the relative velocity at each timestep.

After cycle 5000, a body force is applied in the shear direction in addition to gravity. Theoretically, the corresponding contact force is 25,380 N, and the resulting contact impulse is 1.269 $N \bullet s$. However, since the applied force exceeds the maximum frictional resistance, the Coulomb friction model governs the response, producing 25,292.3 N of friction force and 1.2646 $N \bullet s$ of impulse, which corresponds to a relative displacement of 5.06 $\times$ 10$^{-2}$ mm required to fully mobilize the frictional resistance at the contact interface.

The analysis results showed that all three methods converged to the same analytical value, with convergence patterns similar to those observed in the normal component. In the case of FBM, the shear force gradually increased over approximately 200 cycles and then remained constant after reaching the maximum shear friction (Fig. 4-a). A similar trend was observed in hDEM (Fig. 4-c), where the contact was classified as low-velocity due to negligible change in velocity, confirming that FB-hDEM was applied. In contrast, IBM produced shear impulse corresponding to the maximum shear friction within 2–3 cycles (Fig. 4-b).

Table 2 summarizes the convergence cycle of each method and the relative error ($\epsilon_R$) between the analytical and simulation results at that point. In Eq. (33), $x$ is exact value and $\hat{x}$ is approximated value. Since the test condition is dominated by static contact behavior, the error was calculated based on the contact force, and the convergence was defined when the relative error fell below 5 $\times$ 10$^{-6}$. All methods successfully

**Table 2**
Convergence cycle and relative error of contact force between the analytical solution and simulation results.

| Quantity | Error type | FBM | | IBM | | hDEM | |
|---|---|---|---|---|---|---|---|
| | | Error (%) | Cycle | Error (%) | Cycle | Error (%) | Cycle |
| $F_N$ | Relative error | 4.05 $\times 10^{-4}$ | 397 | 9.58 $\times 10^{-5}$ | 16 | 4.05 $\times 10^{-4}$ | 396 |
| $F_S$ | | 5.34 $\times 10^{-5}$ | 5,161 (161) | 4.03 $\times 10^{-4}$ | 5,003 (3) | 5.69 $\times 10^{-5}$ | 5,161 (161) |

satisfied the convergence criterion in both normal and shear contact forces. However, differences were observed in the number of cycles required to reach convergence. In the normal contact test, FBM and hDEM required approximately 400 cycles to converge, whereas IBM achieved convergence in only 16 cycles. A similar trend was observed in the shear contact test, where FBM and hDEM converged in 161 cycles, while IBM required only 3 cycles.

$$\epsilon_R = \left|\frac{x - \hat{x}}{x}\right| \tag{33}$$

The difference in convergence cycle between methods also leads to discrepancies in shear displacement. In FBM and FB-hDEM, the shear contact force increases gradually, resulting in a corresponding elastic shear displacement (Fig. 5-a, c). In contrast, IBM immediately applies the maximum shear impulse, causing plastic behavior without an elastic phase (Fig. 5-b). These results suggest that IBM is highly efficient in reaching the convergence state, but at the same time less suitable for capturing the detailed joint behavior typically represented by widely used joint models in rock engineering.

### 4.2. Dynamic condition test

The contact response under dynamic impact condition was verified through a free-fall simulation of a block positioned 1 m above the

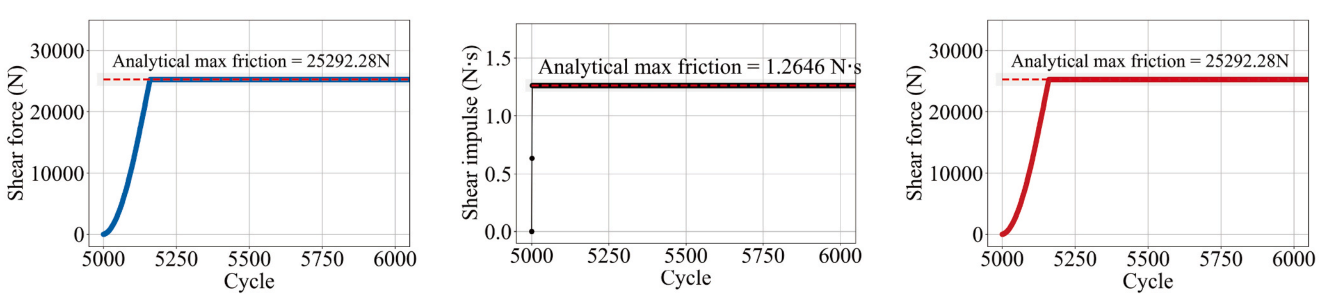


**(a) FBM** **(b) IBM** **(c) hDEM**

**Fig. 4.** Shear component of contact force and impulse.

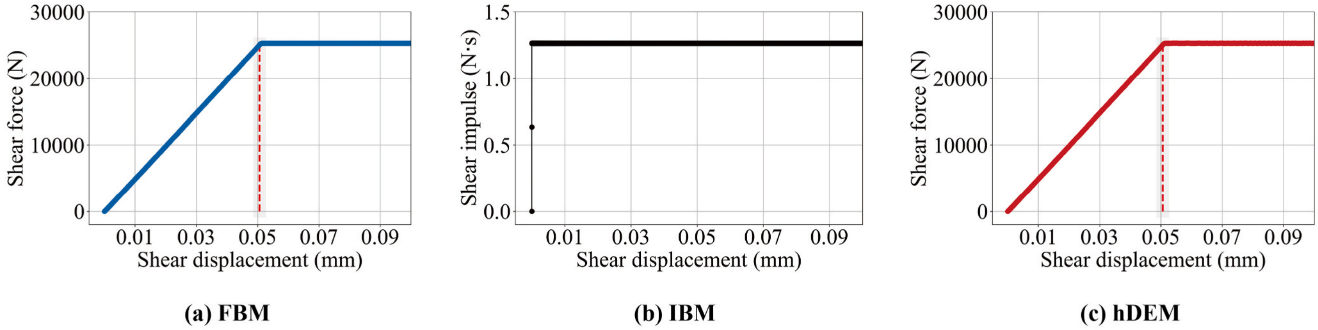


**Fig. 5.** Shear friction-displacement relationship.

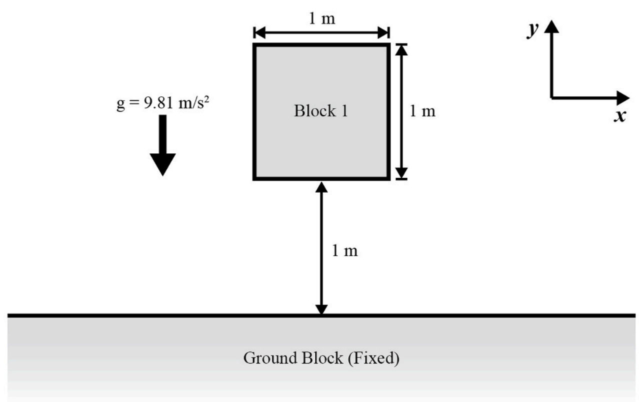


**Fig. 6.** Model description for dynamic contact.

**Table 3**
Model properties for dynamic test.

| Properties | | Unit | Value |
|---|---|---|---|
| Density | | Kg/m3 | 2,700 |
| Joint normal stiffness | | Pa/m | $7 \times 10^9$ |
| Joint shear stiffness | | Pa/m | $5 \times 10^8$ |
| Friction angle | | ° | 15 |
| Cohesion | | Pa | 1e4 |
| Damping coefficient | R | – | 0.5 |
| | α | – | 0.6 |

ground, as illustrated in Fig. 6. The geometry and material properties of block and timestep were kept consistent with those used in the static condition tests (Table 3), except for the damping coefficient (R, α). In addition, damping was applied only during contact to more clearly assess energy conservation in contact calculations; the damping method used during contact was consistent with the formulation defined in each approach.

The results of hDEM and IBM showed identical behavior to the theoretical values, and FBM also produced comparable results by adjusting the damping coefficient (α) (Fig. 7.). In all three methods, initial contact occurred at approximately 0.45 sec after the free fall (around cycle 9,000), confirming that the damping coefficients (R) and post-collision velocities were consistent (Fig. 7-a, b, c). Since damping was not applied during the falling, energy conservation was maintained during this phase (Fig. 7-d, e, f). Upon collision, kinetic energy decreased in proportion to the square of the damping coefficient, demonstrating that the energy dissipation behavior reflected the expected damping characteristics.

Although the difference in velocity and energy responses (Fig. 7) may seem subtle, notable discrepancies exist in terms of numerical stability. The stability of each method was evaluated by applying various timestep sizes (Fig. 8). For FBM, the velocity response was increasingly overestimated with a larger timestep, and stable results could only be obtained when a sufficiently small timestep was used. Especially when block velocities are high, insufficient time resolution can lead to excessive penetration, making FBM sensitive to the trade-off between accuracy and efficiency. In contrast, IBM does not directly rely on penetration depth in its impulse calculation, allowing it to remain stable even at large timesteps. As a result, IBM is more effective for handling high-speed impact problems. Meanwhile, hDEM exhibits intermediate characteristics between FBM and IBM. While it cannot accommodate arbitrarily large timesteps like IBM, it achieves stable results with relatively larger timesteps than FBM, offering a good balance between computational efficiency and numerical accuracy.

Table 4 presents the mean absolute error (MAE) between the analytical solution and the simulation results for different timestep size, calculated over cycle 1 to 30,000, corresponding to a simulation time of 0 to 1.5 sec. In Eq. (34), $x$ is exact value, $\hat{x}$ is approximated value, and $n$ is the sample size. Since this case involves dynamic contact behavior with varying velocities, the error was evaluated based on the velocity response rather than the contact force to appropriately reflect the characteristics of the simulation scenario. At the smallest timestep of $5 \times 10^{-5}$ sec, the MAE of FBM reached 0.045 m/s, while hDEM and IBM exhibited much smaller errors of 0.003 m/s and 0.002 m/s, respectively. This trend was consistently observed across all timestep sizes. As the timestep increased, all methods showed a tendency for the error to increase; however, the increasing rate of error was the smallest in hDEM, with the error growing by 9.79 times as the timestep increased tenfold.

$$MAE = \frac{\sum |x - \hat{x}|}{n} \tag{34}$$

### 4.3. Energy continuity analysis for contact regime transitions

To comprehensively evaluate the energy continuity during contact regime transitions, we conducted a systematic analysis of transition behaviors. in both normal and shear directions for the two possible scenarios: static-to-dynamic and dynamic-to-static transitions.

Dynamic-to-static transitions in the normal direction were examined based on the test in Section 4.2. Initially, high contact velocities triggered IB-hDEM calculations, which gradually decreased with oscillations as the contact converged near the block boundaries. When velocities sufficiently decreased to transition to FB-hDEM, no energy discontinuity was observed. The reverse transition (static-to-dynamic in the normal direction) was not specifically tested, as such conditions would require instantaneous application of extremely large external forces, inherently involving large discontinuous energy changes.

To examine shear direction transitions, the transition behavior was analyzed from the static contact test described in Section 4.1, which minimizes normal component influences by maintaining constant normal overlap throughout the test, ensuring that transition behaviors are primarily governed by shear effects. After reaching the maximum

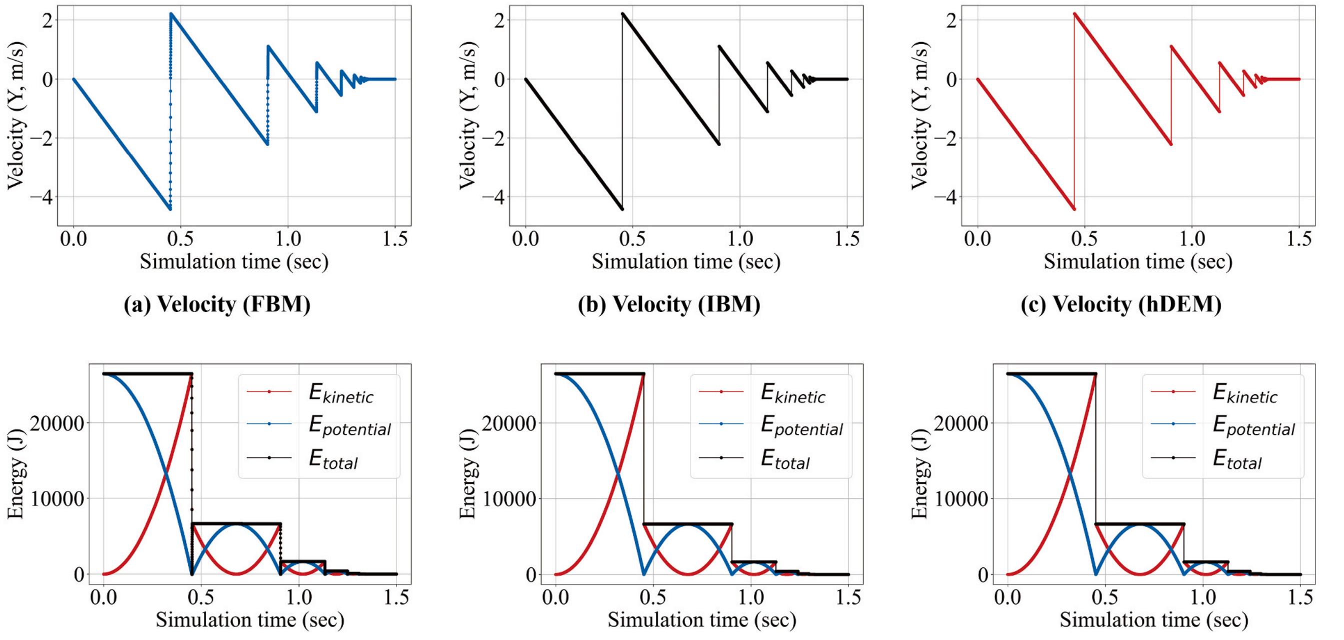


(a) Velocity (FBM) (b) Velocity (IBM) (c) Velocity (hDEM)

(d) Energy (FBM) (e) Energy (IBM) (f) Energy (hDEM)

**Fig. 7.** Velocity and energy of block 1.

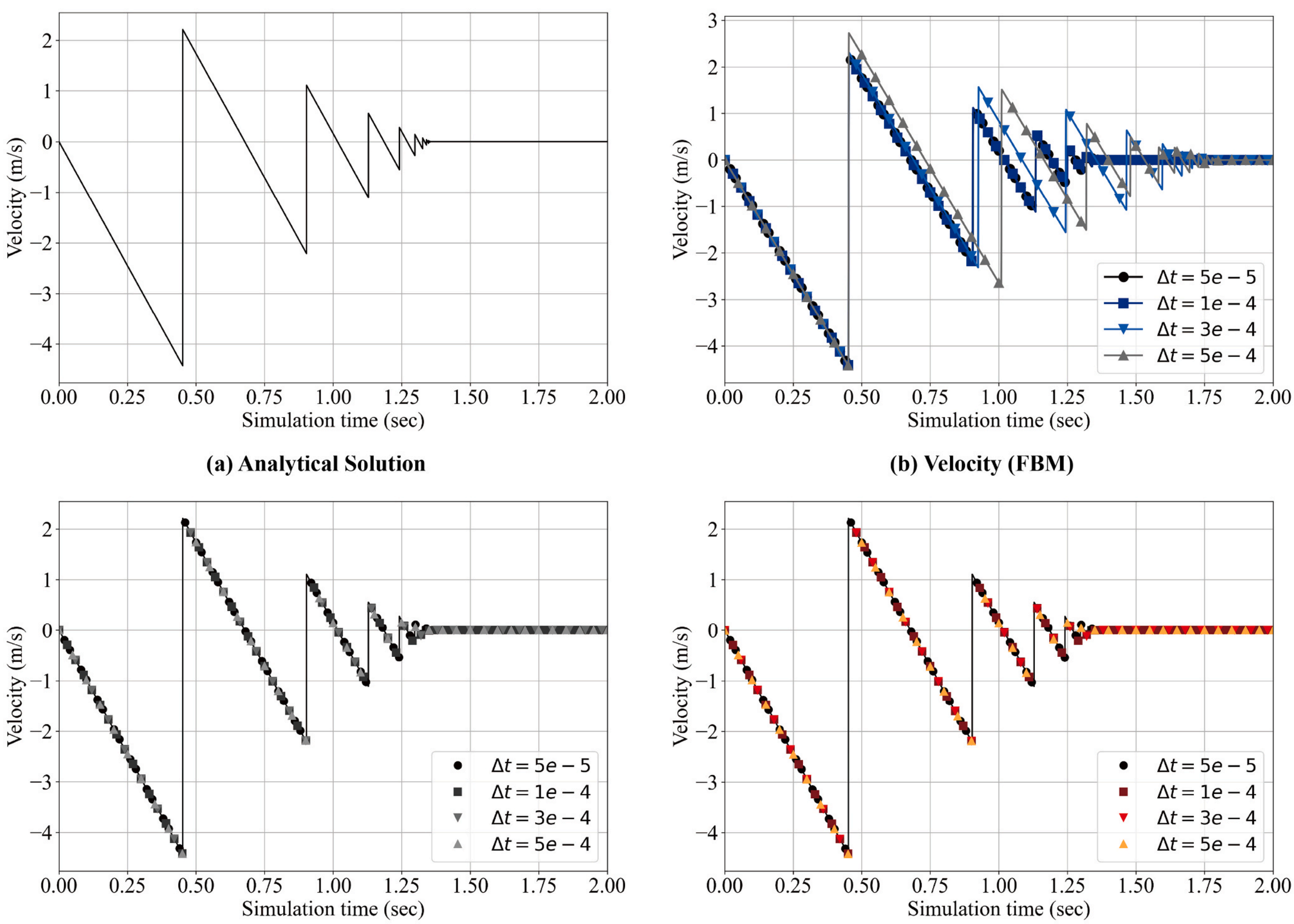


(a) Analytical Solution (b) Velocity (FBM)

(c) Velocity (IBM) (d) Velocity (hDEM)

**Fig. 8.** Comparison of velocity damping during contact under different..$\Delta t$

**Table 4**
MAE between the analytical solution and simulation results with varying timestep.

| Quantity | Timestep (sec) | Error type | Error (Increasing rate from 5e-5 sec) | | |
|---|---|---|---|---|---|
| | | | FBM | IBM | hDEM |
| Velocity (m/s) | $5 \times 10^{-5}$ | MAE | $4.52 \times 10^{-2}$ | $2.24 \times 10^{-3}$ | $3.41 \times 10^{-3}$ |
| | $1 \times 10^{-4}$ | | $4.20 \times 10^{-2}$ (×0.93) | $5.30 \times 10^{-3}$ (×2.37) | $7.11 \times 10^{-3}$ (×2.09) |
| | $3 \times 10^{-4}$ | | $3.41 \times 10^{-1}$ (×7.54) | $1.60 \times 10^{-2}$ (×7.14) | $2.10 \times 10^{-2}$ (×6.16) |
| | $5 \times 10^{-4}$ | | $5.94 \times 10^{-1}$ (×13.1) | $2.51 \times 10^{-2}$ (×11.2) | $3.34 \times 10^{-2}$ (×9.79) |

friction force, the body force acting in the shear direction exceeds the maximum friction force, causing the velocity of Block 1 to gradually increase and eventually surpass the threshold velocity. At this point, hDEM internally switches from FB-hDEM to IB-hDEM. After maintaining this dynamic state for approximately 200 cycles, the shear force was gradually reduced, which caused the velocity of Block 1 to gradually decrease and fall below the threshold velocity. At this point, hDEM switches from IB-hDEM back to FB-hDEM.

To examine whether energy is conserved during this static-to-dynamic transition, the kinetic energy curve of Block 1 was analyzed, revealing a deviation of approximately 0.038 J (2.7 %) around the transition point at cycle 75,300 in Fig. 9. The discrepancy in kinetic energy is attributed to a temporal force gap that occurs during the transition. In the current implementation, the contact force is immediately removed when switching from FB-hDEM to IB-hDEM, whereas the corresponding impulse takes 1–2 cycles to be generated. This transient absence of contact response leads to a momentary increase in velocity, resulting in the observed 2.7 % deviation in kinetic energy.

Dynamic-to-static transitions in the shear direction showed no energy discontinuity, as the gradual velocity reduction allows for smooth transition without force gaps.

While the current implementation shows energy discontinuity only in static-to-dynamic shear transitions, this issue will be addressed in future research through a "soft transition" technique. This approach will gradually reduce the contact force over 2–3 cycles rather than removing it instantaneously, thereby improving energy conservation during contact mode transitions. The soft transition will be applied specifically when static contact has persisted for more than 100 cycles before transitioning to dynamic conditions, ensuring that the technique targets the problematic transition scenario while maintaining computational efficiency.

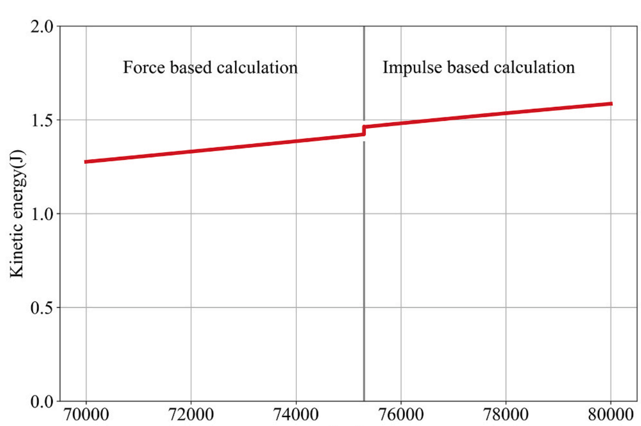


**Fig. 9.** Kinetic energy at the transition point between force-based and impulse-based contact calculation.

### 4.4. Tunnel excavation

A numerical simulation was conducted to evaluate the applicability of hDEM for tunnel excavation in jointed rock masses. Although tunnel excavation is typically considered a quasi-static problem, it may involve localized dynamic behavior if collapse occurs along vulnerable joint surfaces. In this context, the tunnel excavation scenario was selected as an appropriate case study to verify the applicability of hDEM under conditions dominated by quasi-static contacts. Given the nature of this problem, most contacts remained within the quasi-static regime, and hDEM predominantly operated in the FB-hDEM. Accordingly, FBM was selected as the reference method for evaluating mechanical fidelity, as it is conventionally used for problems involving frictional and statically constrained contacts. In contrast, IBM was excluded from this analysis. Its limitations in modeling elastic shear displacement and progressive mobilization of shear resistance, key behaviors in jointed rock masses, have already been demonstrated in Section 4.1. Therefore, further comparison with IBM was deemed unnecessary for the intended purpose of this simulation.

The analysis model consisted of a horseshoe-shaped tunnel with a width of 9 m and a height of 8 m, as shown in Fig. 10. The surrounding rock mass was modeled as a jointed rock with three joint sets, each having a 2° random deviation. The friction angle and cohesion of the joints were reduced to simulate ground condition susceptible to local collapse, as shown in Table 5. The timestep calculated using Eq. (32) was $5.29 \times 10^{-5}$sec. However, as mentioned earlier, a simplified value of $5 \times 10^{-5}$sec was applied for convenience in the verification examples. Consistent with the dynamic test previously described, damping was not applied when blocks were in free fall without contact; however, damping was applied during contact according to the defined scheme for each method. To simulate the excavation process, the central tunnel block was retained until cycle 5,000 to establish the initial ground condition and then removed at cycle 5,000. The convergence criterion was defined as the total kinetic energy when the average velocity of all blocks reached $5 \times 10^{-4}$ m/s, corresponding to a kinetic energy of 0.377 J.

The results showed that, in both methods, six blocks located at the upper-left side of the tunnel detached and fell, indicating similar overall displacement patterns (Fig. 11a, b) measured over the post-excavation convergence period. For a more detailed comparison, the displacements were decomposed into x- and y-directional components (Fig. 11 c–f). Fig. 11-(c) and 11-(d) show the y-direction displacements for FBM and hDEM, respectively. In these figures, red indicates displacement in the positive y-direction, and blue in the negative y-direction. As commonly observed in similar cases, downward displacements occurred at the tunnel roof and upward displacements at the invert, with both methods showing consistent deformation trends, in agreement with the total displacement results.

Figs. 11-(e) and 11-(f) display the x-direction displacements for each method, further confirming the overall similarity. However, localized differences of approximately 0.1–0.2 mm were observed in some regions of side wall, appearing slightly larger in the hDEM results. These differences are attributed to the transition from FB-hDEM to IB-hDEM during the detachment process of the six upper-right blocks. As the falling velocity gradually increases in hDEM, the contact calculation scheme between the falling blocks and adjacent blocks shifts from FB-hDEM to IB-hDEM. Consequently, these contacts disappear within fewer computational cycles, leading to a slight increase in displacement immediately after detachment due to the earlier loss of interaction.

Fig. 12. Compares the contact stresses acting on block interfaces along the tunnel excavation boundary. Six radial profiles were arranged around the boundary, and the contact stresses within 8–10 m along each profile were plotted. The plotted values represent the magnitudes of the stress traction vectors, defined as the vector sum of the normal and shear components of contact stress. Both FBM and hDEM results exhibited similar stress distribution, which was consistent with typical rock mass behavior observed in continuum analysis: High contact stresses were

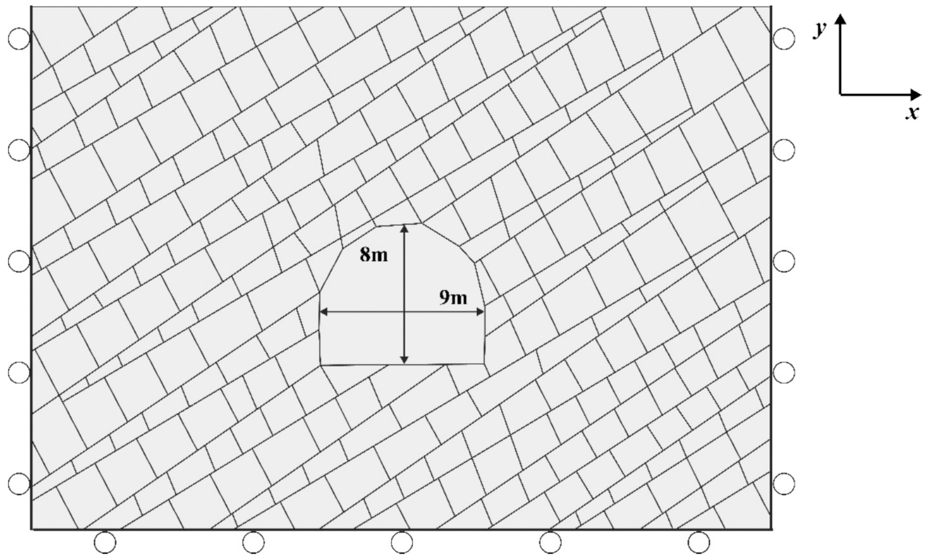


**Fig. 10.** Jointed rock mass model for tunnel excavation test.

**Table 5**
Model properties for tunnel excavation.

| Properties | | Unit | Value |
|---|---|---|---|
| Density | | Kg/m3 | 2,700 |
| Joint normal stiffness | | Pa/m | $7 \times 10^9$ |
| Joint shear stiffness | | Pa/m | $5 \times 10^8$ |
| Friction angle | | ° | 15 |
| Cohesion | | Pa | 1,000 |
| Damping coefficient | R | – | 0.1 |
| | α | – | 0.8 |

observed near the excavation boundary, gradually converging to a relatively constant value with increasing distance, and greater stresses were observed in profiles located at deeper positions (i.e., Profiles 3, 4, and 6) compared to shallower profiles (i.e., Profiles 1, 2, and 5). The similarity between FBM and hDEM results indicates that the contact-adaptive calculation scheme in hDEM does not significantly affect the overall accuracy of the results.

In contrast, significant differences were observed between the two methods in terms of energy dissipation and convergence behavior. Fig. 13 presents the history of total kinetic energy for the entire block system. In the case of FBM, the kinetic energy decreased gradually with large oscillations following the initial contact with the tunnel invert at cycle 28,017 and reached convergence at cycle 99,502. In comparison, hDEM showed a rapid drop in energy after the initial collision at cycle 27,507, reaching convergence much earlier at cycle 37,709 and maintaining a stable low-energy state thereafter.

Table 6 summarizes the key results of the tunnel excavation analysis. The average kinetic energy, average displacement, and maximum displacement were calculated for the blocks adjacent to the excavation surface (i.e. blocks 1–19 as shown in Fig. 12-a), providing an assessment of local response. hDEM converged 65.4 % faster than fDEM, reducing the required number of cycle from 94,502 to 32,709. Despite this significant reduction, the differences in average displacement (0.06 mm) and maximum displacement (0.01 mm) remained minimal. The contact stress distributions were also highly consistent, as previously shown in Fig. 12. This demonstrates that hDEM, by combining the dynamic responsiveness of IBM with the static stability of FBM, can achieve results comparable to fDEM in terms of block behavior while substantially reducing computational cost.

### 4.5. Discussion

This chapter presented a systematic validation of hDEM through four complementary test cases, each designed to evaluate distinct aspects of the proposed framework. The validation strategy progressed from fundamental verification of individual contact regimes to practical demonstration in a geotechnically relevant application.

The static and dynamic contact tests (Sections 4.1 and 4.2) confirmed that hDEM correctly applies FB-hDEM and IB-hDEM based on the threshold velocity criterion, producing results identical to conventional methods under pure static or dynamic conditions. These tests validated the fundamental switching mechanism and demonstrated that the threshold-based classification operates as intended.

The energy continuity analysis (Section 4.3) revealed that regime transitions are generally stable, with only minor energy discontinuities (2.7 %) observed during static-to-dynamic shear transitions. This discontinuity arises from a temporal gap between contact force removal in FB-hDEM and impulse generation in IB-hDEM. To address this limitation, future implementations will incorporate a soft transition technique that gradually attenuates contact forces over 2–3 cycles rather than removing them instantaneously, thereby improving energy conservation during regime switching.

The tunnel excavation simulation (Section 4.4) demonstrated hDEM's primary advantage: significantly improved computational efficiency while maintaining mechanical accuracy. The 65.4 % reduction in convergence cycles represents a substantial performance gain that directly translates to practical benefits in large-scale geotechnical simulations. This improvement stems from hDEM's ability to eliminate prolonged oscillations during dynamic events (such as block detachment) while preserving the detailed mechanical behavior essential for quasi-static analysis. Applying IB-hDEM to dynamic events prevents the prolonged oscillations that characterize conventional FBM simulations under impact conditions, exemplifying the core strength of the hybrid approach.

The results of these foundational validation tests demonstrate that hDEM successfully integrates the computational efficiency of IBM with the mechanical fidelity of FBM, offering a unified framework particularly valuable for problems involving mixed contact regimes. The current study establishes both the conceptual validity and methodological feasibility of the hybrid approach, providing a solid foundation for future extensions to more complex and dynamic scenarios.

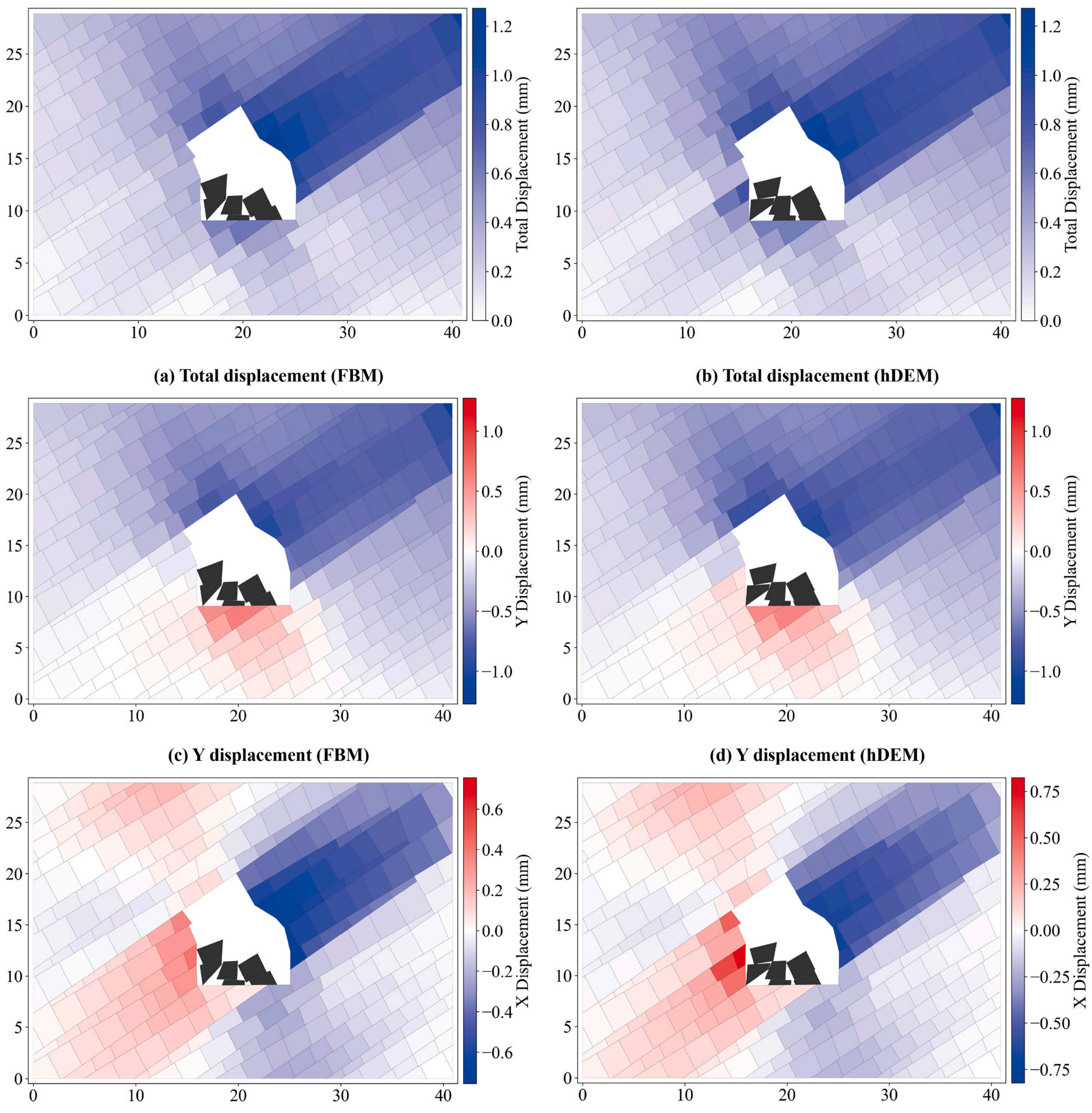


**(a) Total displacement (FBM)** **(b) Total displacement (hDEM)**

**(c) Y displacement (FBM)** **(d) Y displacement (hDEM)**

**(e) X displacement (FBM)** **(f) X displacement (hDEM)**

**Fig. 11.** Displacement and stress distribution using FBM and hDEM.

## 5. Summary and conclusions

In this study, a Hybrid Discrete Element Method (hDEM) was proposed to address the challenges of conventional DEM approaches and to enable more accurate and robust analysis under complex contact conditions. hDEM selectively applies the Force-Based Method (FBM) to quasi-static contacts and the Impulse-Based Method (IBM) to dynamic contacts, depending on the relative contact velocity. This framework allows hDEM to integrate the advantages of both methods while compensating for their respective limitations. To verify the numerical performance of hDEM and evaluate its applicability to geotechnical problems, a series of preliminary numerical simulations was performed, including static and dynamic cases, as well as a tunnel excavation scenario. Based on the numerical simulations, the key features and advantages of hDEM were demonstrated, and its numerical stability, computational efficiency, and potential directions for future research are discussed below.

- hDEM, which classifies contact types based on a threshold velocity, successfully reproduced the results of FBM and IBM under static and dynamic conditions, respectively, showing exact agreement with theoretical values. This capability is particularly beneficial in scenarios where static and dynamic contacts coexist, as demonstrated in the tunnel excavation analysis. In the conventional FBM, the continuous representation of contact using a spring-damper model often results in prolonged vibrations under high-impact conditions,

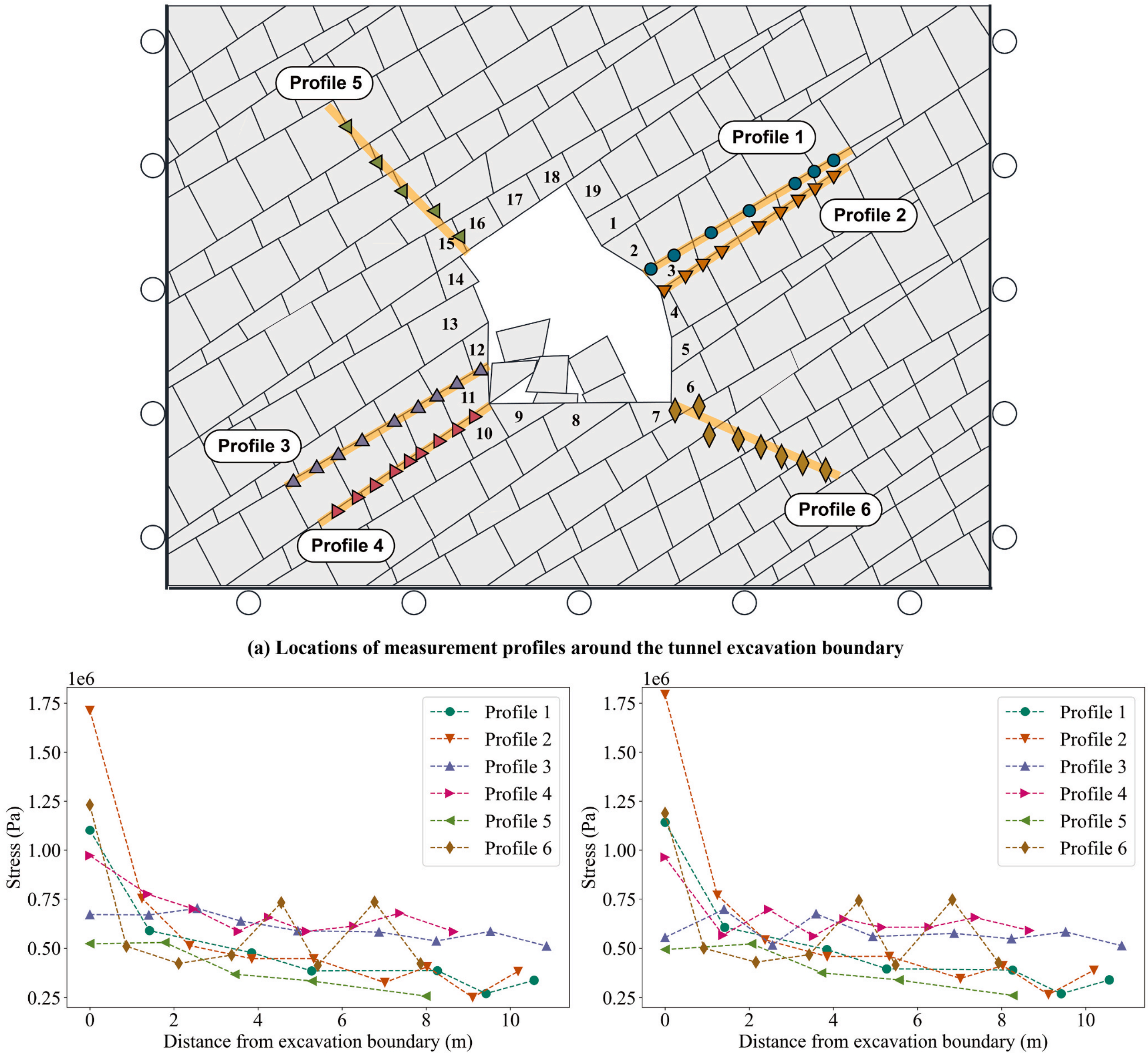


**(a) Locations of measurement profiles around the tunnel excavation boundary**

**(b) Contact stress profiles (FBM)**

**(c) Contact stress profiles (hDEM)**

**Fig. 12.** Comparison of contact stresses along radial profiles from the tunnel excavation boundary.

leading to increased computational costs. In contrast, hDEM achieved comparable results more efficiently and stably by switching to impulse-based calculations when dynamic contacts were detected. This enables more efficient numerical analysis and offers practical benefits for geotechnical engineering applications.

- In several static and dynamic test cases, hDEM yielded results identical to those of FBM and IBM. This indicates that the contact classification algorithm based on threshold velocity operated as intended. Under simplified conditions, such as those used in the tests, hDEM consistently applies a single contact calculation method, depending on the contact type. Consequently, the results naturally align with those of the corresponding conventional method. These findings validate that the internal switching mechanism within hDEM functioned correctly and that the computational schemes were applied as designed.
- The internal transition between FB-hDEM and IB-hDEM was generally stable. However, a slight discontinuity in energy was observed during the switching process. This was attributed to a brief gap in contact reaction that emerged between the removal of contact force in FB-hDEM and the subsequent generation of impulse in IB-hDEM. To mitigate this issue, future research should explore methods to improve the continuity of the contact response across the transition. Such approaches are expected to ensure a more continuous and physically consistent energy response during contact regime switching.
- The threshold velocity proposed in this study was defined based on the maximum velocity that can occur under static contact conditions, and its performance was initially verified through a series of numerical simulations. The proposed approach yielded promising results under the tested conditions, but the current validation is limited to a small number of simplified cases. Therefore, further validation through numerical simulations under more diverse and realistic contact scenarios is planned to enhance the general applicability of hDEM. This includes scenario expansion to problems where dynamic

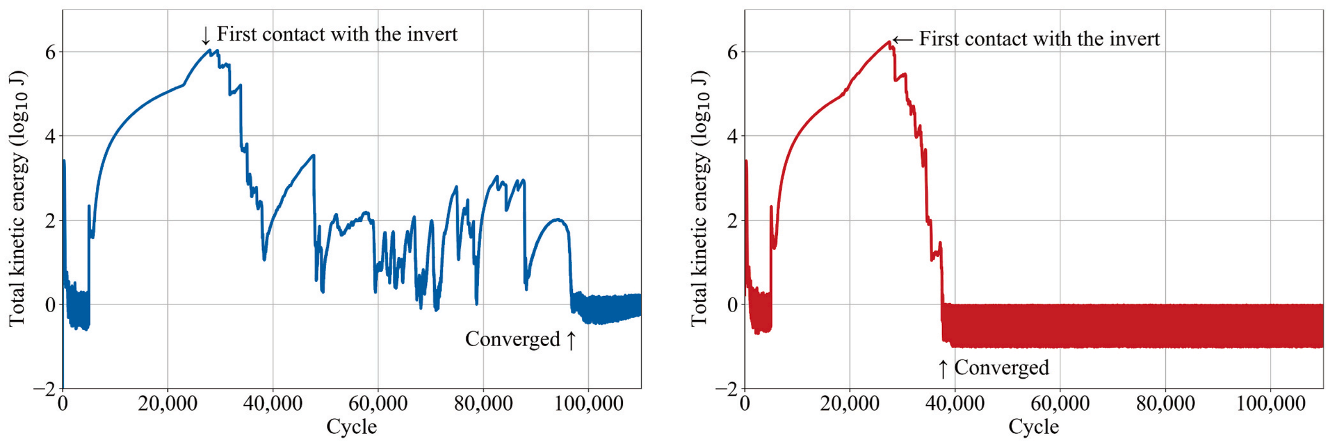


**(a) FBM** **(b) hDEM**

**Fig. 13.** History of total kinetic energy.

**Table 6**
Comparison of convergence behavior for DEM methods.

| State | Unit | FBM | hDEM | Difference |
|---|---|---|---|---|
| Convergence cycle count | Cycle | 94,502 | 32,709 | 61,793 |
| Average kinetic energy | J | $1.96 \times 10^{-8}$ | $4.88 \times 10^{-9}$ | $1.47 \times 10^{-8}$ |
| Average Displacement | mm | 0.64 | 0.7 | 0.06 |
| Maximum displacement | mm | 1.14 | 1.15 | 0.01 |

effects are more dominant, such as impact loading, blast-induced ground motion, and progressive failure in jointed rock masses, as well as validation through field or experimental data comparisons.

- hDEM was developed in the context of two-dimensional mechanical problems, confirming its conceptual feasibility and applicability. On this basis, future work will aim to extend the method to more complex physical environments, including extension to the three-dimensional analysis, where element geometries become more complex and the number of contact events increases significantly, as well as the incorporation of hydro-mechanical (HM) coupling to account for pore water pressure, which plays a critical role in the stability of underground spaces. Through these extensions and further studies, hDEM is expected to evolve into a more practical and reliable analysis method applicable to a wide range of geotechnical and engineering challenges.

## CRediT authorship contribution statement

**Je Kyum Lee:** Writing – original draft, Visualization, Validation, Software, Methodology, Investigation, Formal analysis. **Jorge Loy-Benitez:** Writing – review & editing, Visualization. **Myung Kyu Song:** Writing – review & editing, Validation. **Sean Seungwon Lee:** Writing – review & editing, Supervision, Resources, Funding acquisition, Conceptualization.

## Declaration of competing interest

The authors declare that they have no known competing financial interests or personal relationships that could have appeared to influence the work reported in this paper.

## Acknowledgements

This work was supported by the BK21 FOUR (Fostering Outstanding Universities for Research) program (No. 4299990314624) through the National Research Foundation of Korea (NRF) funded by the Korea Ministry of Education.

## Appendix

*Appendix A*

This appendix presents the derivation of $\dot{u}_{elastic}$, induced by elastic deformation during contact interactions, based on the principle of energy conservation. All variables are defined in the Notations section for clarity.

The elastic potential energy, generated by the spring force during contact, can be decomposed into normal ($E_{p,N}$) and shear ($E_{p,S}$) components, corresponding to normal penetration ($u_N$) and elastic shear deformation ($u_S$), respectively. These components are expressed as:

$$E_{p,N} = \frac{1}{2}K_N u_N^2 \,\&\, E_{p,S} = \frac{1}{2}K_S u_S^2 \tag{A.1}$$

The total kinetic energy ($E_k$) of the two contacting blocks (Block 1 and Block 2) is given by:

$$E_k = \frac{1}{2}m_1\dot{u}_1^2 + \frac{1}{2}m_2\dot{u}_2^2 + \frac{1}{2}I_1\dot{\theta}_1^2 + \frac{1}{2}I_2\dot{\theta}_2^2 \tag{A.2}$$

Assuming that the entire elastic energy stored at the contact is fully converted into kinetic energy without any energy dissipation, and that both blocks are initially at rest:

$$E_{p,N} = E_{k,N} \tag{A.3}$$

$$E_{p,S} = E_{k,S} \tag{A.4}$$

Starting with the normal component, applying energy conservation gives:

$$\frac{1}{2}K_N u_N^2 = \frac{1}{2}m_1 \dot{u}_1^2 + \frac{1}{2}m_2 \dot{u}_2^2 + \frac{1}{2}I_1 \dot{\theta}_1^2 + \frac{1}{2}I_2 \dot{\theta}_2^2 \tag{A.5}$$

Since $K_N$, $u_N$, $m_1$, $m_2$, $I_1$, $I_2$ are either input values or previously computed during DEM simulation, the unknown variables are the velocities. To resolve this, the velocities are expressed in terms of impulse. Let $J_N$ denote the impulse in the normal direction, associated with the conversion of elastic potential energy into kinetic energy:

$$\boldsymbol{J}_N = J_N \widehat{\boldsymbol{n}}_N \tag{A.6}$$

$$J_N = m_{c,N} \left| \Delta \dot{\boldsymbol{u}}_{rel,N} \right| \tag{A.7}$$

Momentum conservation gives:

$$J_N \widehat{\boldsymbol{n}}_N = \Delta\left(m_1 \dot{\boldsymbol{u}}_1\right) \& \boldsymbol{u}_{1\to c} \times (J_N \widehat{\boldsymbol{n}}_N) = \Delta\left(I_1 \dot{\boldsymbol{\theta}}_1\right) \tag{A.8}$$

$$J_N \widehat{\boldsymbol{n}}_N = -\Delta\left(m_2 \dot{\boldsymbol{u}}_2\right) \& \boldsymbol{u}_{2\to c} \times (J_N \widehat{\boldsymbol{n}}_N) = -\Delta\left(I_2 \dot{\boldsymbol{\theta}}_2\right) \tag{A.9}$$

Change of velocity can be written as:

$$\Delta \dot{\boldsymbol{u}}_1 = \frac{J_N \widehat{\boldsymbol{n}}_N}{m_1} \& \Delta\ \dot{\boldsymbol{\theta}}_1 = J_N \frac{\boldsymbol{u}_{1\to c} \times \widehat{\boldsymbol{n}}_N}{I_1} \tag{A.10}$$

$$\Delta \dot{\boldsymbol{u}}_2 = -\frac{J_N \widehat{\boldsymbol{n}}_N}{m_2} \& \Delta\ \dot{\boldsymbol{\theta}}_2 = -J_N \frac{\boldsymbol{u}_{2\to c} \times \widehat{\boldsymbol{n}}_N}{I_2} \tag{A.11}$$

Since the initial velocities are zero:

$$\Delta \dot{\boldsymbol{u}}_1 = \dot{\boldsymbol{u}}_1 \& \Delta \dot{\boldsymbol{u}}_2 = \dot{\boldsymbol{u}}_2 \& \Delta \dot{\boldsymbol{\theta}}_1 = \dot{\boldsymbol{\theta}}_1 \& \Delta \dot{\boldsymbol{\theta}}_2 = \dot{\boldsymbol{\theta}}_2 \tag{A.12}$$

Substituting Eqs. (A.10)-(A.12) into Eq. (A.5):

$$\begin{aligned} \frac{1}{2}K_N u_N^2 = \frac{1}{2}m_1 \left(\frac{J_N \widehat{\boldsymbol{n}}_N}{m_1}\right)^2 + \frac{1}{2}m_2 \left(-\frac{J_N \widehat{\boldsymbol{n}}_N}{m_2}\right)^2 + \frac{1}{2}I_1 \left(J_N \frac{\boldsymbol{u}_{1\to c} \times \widehat{\boldsymbol{n}}_N}{I_1}\right)^2 \\ + \frac{1}{2}I_2 \left(-J_N \frac{\boldsymbol{u}_{2\to c} \times \widehat{\boldsymbol{n}}_N}{I_2}\right)^2 \end{aligned} \tag{A.13}$$

$$K_N u_N^2 = J_N^2 \left\{ \frac{1}{m_1} + \frac{1}{m_2} + \frac{|\boldsymbol{u}_{1\to c} \times \widehat{\boldsymbol{n}}_N|^2}{I_1} + \frac{|\boldsymbol{u}_{2\to c} \times \widehat{\boldsymbol{n}}_N|^2}{I_2} \right\} \tag{A.14}$$

Let the collision mass ($m_{c,N}$) be defined as:

$$\frac{1}{m_{c,N}} = \frac{1}{m_1} + \frac{1}{m_2} + \frac{|\boldsymbol{u}_{1\to c} \times \widehat{\boldsymbol{n}}_N|^2}{I_1} + \frac{|\boldsymbol{u}_{2\to c} \times \widehat{\boldsymbol{n}}_N|^2}{I_2} \tag{A.15}$$

$$K_N u_N^2 = \frac{J_N^2}{m_{c,N}} \tag{A.16}$$

$$K_N u_N^2 = \frac{m_{c,N}^2 \left| \Delta \dot{\boldsymbol{u}}_{rel,N} \right|^2}{m_{c,N}} \tag{A.17}$$

$$\left| \Delta \dot{\boldsymbol{u}}_{rel,N} \right| = \sqrt{\frac{K_N u_N^2}{m_{c,N}}} \tag{A.18}$$

Similarly, for the shear component:

$$\left| \Delta \dot{\boldsymbol{u}}_{rel,S} \right| = \sqrt{\frac{K_S u_S^2}{m_{c,S}}} \tag{A.19}$$

$$\frac{1}{m_{c,S}} = \frac{1}{m_1} + \frac{1}{m_2} + \frac{|\boldsymbol{u}_{1\to c} \times \widehat{\boldsymbol{n}}_S|^2}{I_1} + \frac{|\boldsymbol{u}_{2\to c} \times \widehat{\boldsymbol{n}}_S|^2}{I_2} \tag{A.20}$$

Note that in Eq. (A.19) $u_S$ represents the elastic deformation caused by the frictional force (not the entire shear displacement), which is defined as:

$$u_S = \frac{F_{friction}}{K_S} \tag{A.21}$$

Since initial velocities are zero, the magnitude of the relative velocity due purely to elastic energy is:

$$\left|\dot{\boldsymbol{u}}_{elastic}\right| = \left|\dot{\boldsymbol{u}}_{rel,N} + \dot{\boldsymbol{u}}_{rel,S}\right| = \left|\Delta\dot{\boldsymbol{u}}_{rel,N} + \Delta\dot{\boldsymbol{u}}_{rel,S}\right| = \sqrt{\frac{K_N u_N^2}{m_{c,N}} + \frac{K_S u_S^2}{m_{c,S}}} \tag{A.22}$$

## Data availability

Data will be made available on request.

## References


Augrade, C.E., Lee, S.J., Loukidis, D., 2021. Numerical modelling of the deformation problems in geotechnical engineering: a state-of-the-art review. Soils Found. 61, 1718–1735. https://doi.org/10.1016/j.sandf.2021.08.007.

Baraff, D., 1997a. An Introduction to Physically based Modeling: rigid Body simulation I - Unconstrained rigid Body Dynamics. SIGGRAPH Course. Notes.

Baraff, D., 1997b. An Introduction to Physically based Modeling: rigid Body simulation II - Nonpenetration Constraints. SIGGRAPH Course. Notes.

Baraff, D., 1989. Analytical Methods for Dynamic simulation of Non-Penetrating rigid Bodies. Computer Graphics 23 (3), 223–232. https://doi.org/10.1145/74334.74356.

Barbosa-Carrillo, R.E., 1990. Discrete element models for granular materials and rock masses. University of Illinois at Urbana-Champaign. Ph.D. thesis.

Barton, N., 1973. Review of a new shear-strength criterion for rock joints. Eng. Geol. 7, 287–332. https://doi.org/10.1016/0013-7952(73)90013-6.

Barton, N., Choubey, V., 1977. The shear strength of rock joints in theory and practice. Rock Mech. Rock Eng. 10, 1–54. https://doi.org/10.1007/BF01261801.

Barton, N., 1982. Modelling rock joint behavior from in situ block test: implications for nuclear waste repository design. ONWI-308. prepared by Terra Tek, Inc. Battelle Memorial Institute, Columbus, OH.

Catto, E., Park, M., 2005. Iterative Dynamics with Temporal Coherence. Game Developer Conference.

Catto, E., 2009. Modeling and Solving Constraints. Game developers conference.

Cundall, P.A., 1988. Formulation of a 3-Dimensional Distinct Element Model. 1. a Scheme to Detect and Represent Contacts in a System Composed of many Polyhedral Blocks. International Journal of Rock Mechanics and Mining Sciences & Geomechanics Abstracts 25, 107–116. https://doi.org/10.1016/0148-9062(88)92293-0.

Cundall, P.A., 1987. Distinct element methods of rock and soil structure, in: Brown, E.T., Analytical and computational methods in engineering rock mechanics. Allen and Unwin, London, pp. 129-163.

Cundall, P.A., Hart, R., 1992. Numerical modeling of discontinua. Engineering computations 9, 101–113. https://doi.org/10.1108/eb023851.

Cundall, P.A., Strack, O.D.L., 1979. Discrete Numerical-Model for Granular Assemblies. Geotechnique 29, 47–65. https://doi.org/10.1680/geot.1979.29.1.47.

Duriez, J., Bonelli, S., 2021. Precision and computational costs of Level Set-Discrete Element Method (LS-DEM) with respect to DEM. Comput. Geotech. 134, 104033. https://doi.org/10.1016/j.compgeo.2021.104033.

Fukuda, D., Liu, H., Zhang, Q., Zhao, J., Kodama, J., Fujii, Y., Chan, A.H.C., 2021. Modelling of dynamic rock fracture process using the finite-discrete element method with a novel and efficient contact activation scheme. Int. J. Rock Mech. Min. Sci. 138, 104645. https://doi.org/10.1016/j.ijrmms.2021.104645.

Hahn, J.K., 1988. Realistic animation of rigid bodies. Computer Graphics 22, 299–308. https://doi.org/10.1145/378456.378530.

Hart, R., Cundall, P.A., Lemos, J., 1988. Formulation of a 3-Dimensional Distinct Element Model. 2. Mechanical Calculations for Motion and Interaction of a System Composed of many Polyhedral Blocks. International Journal of Rock Mechanics and Mining Sciences & Geomechanics Abstracts 25, 117–125. https://doi.org/10.1016/0148-9062(88)92294-2.

Hoek, E., Brown, E.T., 1980. Underground Excavations in Rock. CRC Press.

Izadi, E., Bezuijen, A., 2018. Simulating direct shear tests with the bullet physics library: a validation study. PLoS One 13, e0195073. https://doi.org/10.1371/journal.pone.0195073.

Jing, L., 2003. A review of techniques, advances and outstanding issues in numerical medelling for rock mechanics and rock engineering. International Journal for Rock Mechanics and Mining Sciences 40, 283–353. https://doi.org/10.1016/S1365-1609(03)00013-3.

Jing, L., Hudson, J.A., 2002. Numerical methods in rock mechanics. International Journal for Rock Mechanics and Mining Sciences 39, 409–427. https://doi.org/10.1016/S1365-1609(02)00065-5.

Kavan, L., 2003. Rigid Body Collision Response. In Proceedings of the 7th Central European Seminar on Computer Graphics.

Ladanyi, B., Archambault, G., 1969. Simulation of Shear Behavior of a Jointed Rock Mass. Presented at the The 11th U.S. Symposium on Rock Mechanics (USRMS).

Lee, S., 2003. Stability around underground openings in rock with dilative, non-persistent and multi-scale wavy joints using a discrete element method. University of Illinois at Urbana-Champaign. Ph.D. thesis.

Lee, S.J., 2014. Developments in large scale discrete element simulations with polyhedral particles. University of Illinois at Urbana-Champaign, University of Illinois at Urbana-Champaign. Ph.D. thesis.

Lee, S.J., Hashash, Y.M.A., 2015. iDEM: an impulse-based discrete element method for fast granular dynamics. Int. J. Numer. Meth. Eng. 104, 79–103. https://doi.org/10.1002/nme.4923.

Lei, Y., Liu, Q., Liu, H., 2025. Developing a memory-efficient GPGPU-parallelized contact detection algorithm for 3D engineering-scale FDEM simulations. Comput. Geotech. 179, 107031. https://doi.org/10.1016/j.compgeo.2024.107031.

Lemos, J.V., 2012. Recent developments and future trends in distinct element methods-UDEC/3DEC and PFC codes, in: Zhao, J., Zhao, G. Sasaki, T., Advances in Discontinuous Numerical Methods and Applications in Geomechanics and Geoengineering. Taylor and Francis Group, London, pp. 17-29.

Li, Y., Asai, M., Chandra, B., Isshiki, M., 2021. Energy-tracking impulse method for particle-discretized rigid-body simulations with frictional contact. Computational Particle Mechanics 8, 237–258. https://doi.org/10.1007/s40571-020-00326-5.

Lisjak, A., Grasselli, G., 2014. A review of discrete modeling techniques for fracturing process in discontinuous rock masses. J. Rock Mech. Geotech. Eng. 6, 301–314. https://doi.org/10.1016/j.jrmge.2013.12.007.

Lubbe, R., Xu, W.-J., Wilke, D.N., Pizette, P., Govender, N., 2020. Analysis of parallel spatial partitioning algorithms for GPU based DEM. Comput. Geotech. 125, 103708. https://doi.org/10.1016/j.compgeo.2020.103708.

Mirtich, B.V., 1996. Impulse-based Dynamic simulation of rigid Body Systems. University of California at Berkeley. Ph.D. thesis.

Paluszny, A., Tang, X., Zimmerman, R.W., 2013. Fracture and impulse based finite-discrete element modeling of fragmentation. Comput. Mech. 52, 1071–1084. https://doi.org/10.1007/s00466-013-0864-5.

Park, E.H., Kindratenko, V., Hashash, Y.M.A., 2021. Shared memory parallelization for high-fidelity large-scale 3D polyhedral particle simulations. Comput. Geotech. 137, 104008. https://doi.org/10.1016/j.compgeo.2021.104008.

Patton, F.D., 1966. Multiple modes of shear failure in rock and related materials. In: Ph, D. (Ed.), thesis. Department of Earth Sciences. The University of Leeds.

Plesha, M.E., 1987. Constitutive models for rock discontinuities with dilatancey and surface degradation. Int. J. Numer. Anal. Meth. Geomech. 11, 345–362. https://doi.org/10.1002/nag.1610110404.

Schneider, H.J., 1976. The friction and deformation behaviour of rock joints. Rock Mech. 8, 169–184. https://doi.org/10.1007/BF01239813.

Stevens, A.B., Hrenya, C.M., 2005. Comparison of soft-sphere models to measurements of collision properties during normal impacts. Powder Technol. 154, 99–109. https://doi.org/10.1016/j.powtec.2005.04.033.

Tan, P., Wijesuriya, H.S., Sitar, N., 2024. 3-D impulse-based level-set method for granular flow modeling. Int. J. Numer. Meth. Eng. 125, e7546.

Thornton, C., 1997. Coefficient of Restitution for Collinear Collisions of Elastic-Perfectly Plastic Spheres. J. Appl. Mech. 64, 383–386. https://doi.org/10.1115/1.2787319.

Tsuji, Y., Tanaka, T., Ishida, T., 1992. Lagrangian numerical simulation of plug flow of cohesionless particles in a horizontal pipe. Powder Technol. 71, 239–250. https://doi.org/10.1016/0032-5910(92)88030-L.

Wang, T., Zhang, F., Furtney, J., Damjanac, B., 2022. A review of methods, applications and limitations for incorporating fluid flow in the discrete element method. J. Rock Mech. Geotech. Eng. 14, 1005–1024. https://doi.org/10.1016/j.jrmge.2021.10.015.

Wang, Z., Li, F., Mei, G., 2024. OpenMP Parallel Finite-Discrete Element Method for Modeling Excavation support with Rockbolt and Grouting. Rock Mech. Rock Eng. 57, 3635–3657. https://doi.org/10.1007/s00603-023-03746-w.

Zhang, B., Han, B., Zhang, Q., 2024. An improved GPU-Parallelized 2D/3D Elastoplastic-Damage-Fracture Joint Framework for combined Finite–Discrete-Element Program. Rock Mech. Rock Eng. 57, 3971–3991. https://doi.org/10.1007/s00603-023-03738-w.

Zhou, W., Ma, X., Ng, T.-T., Ma, G., Li, S.-L., 2016. Numerical and experimental verification of a damping model used in DEM. Granul. Matter 18, 1. https://doi.org/10.1007/s10035-015-0597-6.